

A Comparative Study of High Temperature Tensile and Creep Testing Between Standard and Miniature Specimens: Applicability and Limits



YUANBO T. TANG, CASPAR SCHWALBE, MAGDALENA FUTOMA, BRYAN ROEBUCK, SATOSHI UTADA, and ROGER C. REED

This study concerns the quasi-static and time-dependent mechanical behavior obtained *via* the miniaturized electro-thermal mechanical testing (ETMT) approach for single crystal (SX) and conventional cast Mar-M-247 superalloy. The experimental outcome was benchmarked against standardized testing procedures. It is found that tensile yielding behavior can be captured accurately by the ETMT approach up to 1100 °C, provided the appropriate type of thermocouple (T/C) is chosen. Furthermore, creep rupture behavior is underestimated by the miniaturized set-up. High repeatability of the rupture time was obtained for the SX case, whereas a significant scatter was observed for the conventional cast case. The discrepancies are assessed in detail; discussion centers around analytical and practical considerations, such as temperature uncertainty due to parasitic voltage and the choice of T/C, microstructural change as a result of the Joule heating, representative gauge volume, and strain rate non-linearity. Consequently, the applicability and limits of the miniaturized approach are examined critically, and improvements were suggested where appropriate.

<https://doi.org/10.1007/s11661-022-06869-x>
© The Author(s) 2022

I. INTRODUCTION

AVIATION is evolving tremendously in recent years toward the sustainability goal as evidenced by a number of eco-travel initiatives and proposals.^[1,2] Innovation using alternative power system utilizing electricity, hydrogen fuel, or hybrid approaches are currently under consideration.^[3–7] Although it is still early to pinpoint the solution which will emerge, it is clear that the modern trend in the usage of nickel-based superalloys is moving toward thinner and smaller components with cross-sectional thickness of approximately 1 to 2 mm, which facilitates lightweighting of the structures and improved cooling efficiencies and aerodynamics. This situation calls into question the traditional reliance on standardized tensile and creep testing for life assessment.

First, the surface-to-volume ratio is not necessarily representative of the component and its application. Second, local microstructural heterogeneity that arises from thermal mechanical history *via* investment casting differs.^[8] Third, from a practical perspective, sometimes the standardized samples cannot be extracted from a thin-walled product as it requires a much larger piece of material for machining. Therefore, timely development of robust small-scale mechanical characterization for lifing of (intricate) thin-walled structures is urgently needed.

Miniaturized mechanical testing is not new,^[9–11] however, it has not received strong traction scholarly or industrially in the past. The conventional wisdom is that reproducibility is very important so that approaches such as American Society for Testing and Materials (ASTM) and the like are taken as gold standard. Miniaturized tests, on the other hand, are usually modified for specialized laboratory-based evaluation.^[10,12–15] Such measurements are self-consistent and allow for ranking of materials and alloy grades; but it does not necessarily produce universally recognized comparison between standardized testing, because of variation in procedures from system to system, certain assumptions must take place and also there is an intrinsic thickness debt effect.^[16–19] The practitioners in the field utilize miniaturized testing as a benchmark test for rapid screening, which still needs a confirmation with

YUANBO T. TANG, SATOSHI UTADA, and ROGER C. REED are with the Department of Materials, University of Oxford, Parks Road, Oxford OX1 3PH, UK. Contact e-mail: yuanbo.tang@materials.ox.ac.uk CASPAR SCHWALBE and MAGDALENA FUTOMA are with the MTU Aero Engines AG, Dachauer Str. 665, Munich, Germany. BRYAN ROEBUCK is with the National Physical Laboratory, Hampton Road, Teddington, Middlesex TW11 0LW, UK.

Manuscript submitted July 31, 2022; accepted October 14, 2022.

Article published online November 5, 2022

additional ASTM testing for proof. With the shifting paradigm of thin-wall structural applications, the need for future miniaturized testing market must be fulfilled—aiming for stand-alone qualification as a mainstream technique. It is timely to re-evaluate such methodologies in a critical way for future development and standardization.

In this work, we conduct a comprehensive assessment of the electro-thermal mechanical testing (ETMT) system and its utilization in tensile and creep tests up to 1100 °C for both single crystal (SX) and conventional cast superalloys. The aim is to review the procedures and key assumptions with rigor and accurately pinpoint the applicability and limitations. Some testing conditions are deliberately chosen to push the envelope and even to invalidate assumptions. Another independent set of tests were carried out at MTU Aero Engines AG (Germany) under ASTM procedures with the same batch of materials, to allow the ETMT results to be assessed critically. The discrepancies are analyzed in detail; error sources such as uncertainty in strain rate, choice of thermocouple (T/C) type, representative gauge volume, and parasitic voltage are discussed thoroughly. Effects of surface-to-volume ratio and environmental damage on deformation are also considered. Further improvements are suggested to minimize the discrepancy induced from ETMT miniaturized testing. This work contributes to the timely and significant subject of miniaturized testing of structural materials at high temperature, raising its potential for application to thin-walled components.

II. ETMT TESTING: CAPACITIES AND ASSUMPTIONS

The ETMT system was invented at the National Physical Laboratory (NPL) UK in 2001,^[20] with its subsequent commercialization by Instron Ltd.^[21] The core functionalities of the testing system involve a dynamic loading frame with heating capacity. Similar to a Gleeble type thermal mechanical machine, heating is delivered by DC electric current, *i.e.*, Joule heating, hence the term electro-thermal. By contrast, the specimen cross-section is much smaller than for the Gleeble samples, typically within the range of $1 \times 1 \times 3$ or $2 \times 2 \times 3$ mm³ thus the skin effect is minimal and a homogeneous cross-section temperature distribution can be achieved more readily. Samples are gripped by two water cooled crossheads with a separation of 16 mm. A parabolic temperature profile is established along the loading direction, where the central 3 mm reaches local temperature equilibrium and is considered as the effective gauge length.^[22] Due to the Joule heating method, it is possible to achieve thermal cycling rate as high as 100 K/s making it suitable to study non-equilibrium microstructure.^[23] For the experimental set-up in this study, strain measurements are conducted using non-contact extensometry using iMetrum Video Gauge software within an environmental chamber in

laboratory air, argon, or in vacuum. The details of the test set-up used in this study are provided in Reference [22].

In order to obtain representative and repeatable results, certain caveats need to be added.

- (1) T/C location and quality
T/Cs are made individually for each test in bare wire configuration. They must be spot welded at the center of the specimen such that the distance to each crosshead is the same. This ensures the monitored temperature is within the assumed local temperature equilibrium (the central 3 mm). In addition, it is assumed the temperature is uniformly distributed across the gauge where geometrical effect is ignored, *i.e.*, no difference in temperature between the surface, corners, or the bulk. A large specimen size will invalidate this assumption. Furthermore, a high-quality T/C bead is essential to minimize the parasitic voltage effect, *i.e.*, no oxidation and remains roughly spherical, instead of one wire spot welded on top of another. The error induced by parasitic voltage can be up to 100 K for Type R and 30 K for Type K at 700 °C.^[21] An easy and robust way to spot the existence of significant parasitic voltage is to record current density (A/mm²) at certain temperature increments. Abnormal reading can immediately flag out inappropriate tests although this requires pre-existing knowledge of the material's response during testing.
- (2) Gauge length, sampling volume, and strain rate
For ambient testing, the gauge volume is defined by the parallel length and cross-sectional area. However, this alters when one carries out tests at high temperature. Since the specimen has a local temperature equilibrium at the center 3 mm length, which is taken as the true gauge length, despite the parallel section is actually much longer. For a high temperature test to be valid, one can assume the materials strength decreases monotonically with temperature. This allows for the middle 3 mm gauge to take deformation despite having the same cross-sectional area. If anomalous yielding exists, the out-of-gauge section will yield first,^[22] where the gauge may never deform sufficiently for measurements to take place. Testing of [001] oriented Ni-based SX superalloy at 750 °C in this study has intentionally violated this assumption, with discussion takes place in Section V-A-ii. Moreover, strain measurement becomes less accurate when local necking onsets, for nickel alloys this is typically at 20 pct engineering strain or greater. Furthermore, for representative sampling volume, one typically needs 100 grains or more at the cross-section to obtain an average response consistent with homogeneity. For a typical sample design of $1 \times 1 \times 3$ mm³ gauge volume, it leads to a grain size of 100 μm or less being the limit. Larger than this, one expects a significant scatter in results, arising from material heterogeneity. Moreover, since the gauge is defined only as the central 3 mm, it is hard to use a clip-on extensometer, both for

location accuracy and heat conduction reasons. The iMetrum video extensometer system in the set-up cannot be used as a control channel due to insufficient feedback rate. Hence, for the set-up used in the current study, one can preset a displacement speed *via* linear variable differential transformer (LVDT) to correlate with the true strain rate.

(3) Heating method: Joule heating *vs.* radiation heating

In contrast to a conventional furnace with radiation heating, the heating system in the ETMT utilizes a large DC current, hence the material to be tested must be electrically conductive. Despite Joule heating being commonly used in laboratory-based facilities such as Gleeble thermomechanical simulator^[24] and pulsed electric current sintering (PECS),^[25] it is known that significant current density may influence the behavior of metals and alloys. There have been a few reports on Al,^[26] Cu,^[27] and Ni alloys,^[28] in which applied current facilitates solid-state phase transformation kinetics, such as recovery and recrystallization. Although the phenomenon is known, it has not been quantitatively understood and has been neglected generally. For quasi-static testing, this assumption is likely to be reasonable, however, for testing with extended period, further evaluation is needed.

III. EXPERIMENTAL METHODOLOGIES

Mar-M-247 nickel-based superalloy was used in the current study. Its nominal composition is shown in Table 1. The material was processed from two separate routes in MTU Aero Engines, *i.e.*, polycrystalline (PX) by conventional cast and [001] orientation SX. Each casting method utilized the material from the same master heat; no chemical outliers were determined from the manufacturer. Both types of materials were subject to mechanical testing carried out using ETMT and ASTM procedures at Oxford and MTU Aero Engines, respectively. Standard heat treatment was applied prior to machining and testing, where solid solution treatment was carried out at 1185 °C/2 h followed by aging at 871 °C/20 h. Optical microscope revealed the grain size of the PX Mar-M-247 is equivalent to ASTM 3 or ~ 130 μm. The [001] SX bars for ETMT and ASTM testing came from the same mold, which crystal orientations exhibiting less than 3 deg difference.

A. ETMT Testing Procedures

ETMT samples were first extracted using electro discharge machining (EDM) process into dedicated geometries. For tensile tests, the specimen is 40 mm long with the parallel section being 1 × 1 × 14 mm³; for creep tests, the specimen length is also 40 mm with the parallel section being 2 × 2 × 10 mm³, detailed drawings used for the current study can be found elsewhere.^[22,23]

The specimens were first ground using abrasive media up to 4000 grit, measured using a micrometer for cross-sectional dimensions with a precision of 1 μm. Subsequently, the speckle patterns were applied on the surface of the specimens for video extensometer tracking; specifically flame proof with very high temperature paints were used—white paint was applied uniformly first to cover the whole surface and then black paint was sprayed on top to form speckles—reverse order between the paints achieves the same result. The speckle patterns remain visible at 1100 °C or higher. The video was stored and post analyzed using an iMetrum system. The camera acquisition rate for tensile testing was 10 Hz. A Type K T/C was spot welded in the center of the specimen for temperature control; its wire thickness was 0.125 mm. A Type R T/C of the same wire thickness was used in a later stage for SX tensile testing at 1100 °C. A strain rate close to 0.5 pct/min ($8.3 \times 10^{-5} \text{ s}^{-1}$) was employed for all testing at 25 °C, 750 °C, 980 °C, and 1100 °C until failure. Creep testing was carried out until failure in the same set-up with an acquisition rate of 0.1 Hz. Two creep conditions were evaluated, *i.e.*, 850 °C/550 MPa and 980 °C/200 MPa. All tensile and creep tests were repeated for three times.

B. ASTM Testing Procedures

Standardized testing was carried out in accordance with ASTM procedures, thus specimens were manufactured to comply with ASTM E8M specifications with a gauge diameter of 6 mm and a gauge length of 30 mm. The gauge diameter was measured with a precision of 0.01 mm. Testing conditions were identical to the ETMT tests as described above, *i.e.*, tensile tests at 25 °C, 750 °C, 980 °C, and 1100 °C and creep tests at 850 °C/550 MPa and 980 °C/200 MPa. For tensile testing, a clip-on extensometer was applied, where the strain rate was 0.5 pct/min ($8.3 \times 10^{-5} \text{ s}^{-1}$). The extensometer was removed after the yield point can be determined. When the extensometer was removed, the strain control was changed from extensometer to displacement rate, hence a small ‘jump’ or ‘drop’ in the tensile curve may be captured during the switch over. For creep test, all samples were interrupted at 2 pct creep strain. Three tests were carried out at each condition, apart from only one sample was tested at 25 °C and no PX material was tested at 1100 °C.

Table 1. Nominal Composition of Mar-M-247 for Current Study in Wt Pct (Ni-Base)

	Ni	Cr	Co	Al	Ti	Ta	W	Mo	Hf	Zr	C	B
Mar-M-247	balance	8.4	10.0	5.5	1.0	3.0	10.0	0.7	1.5	0.05	0.15	0.015

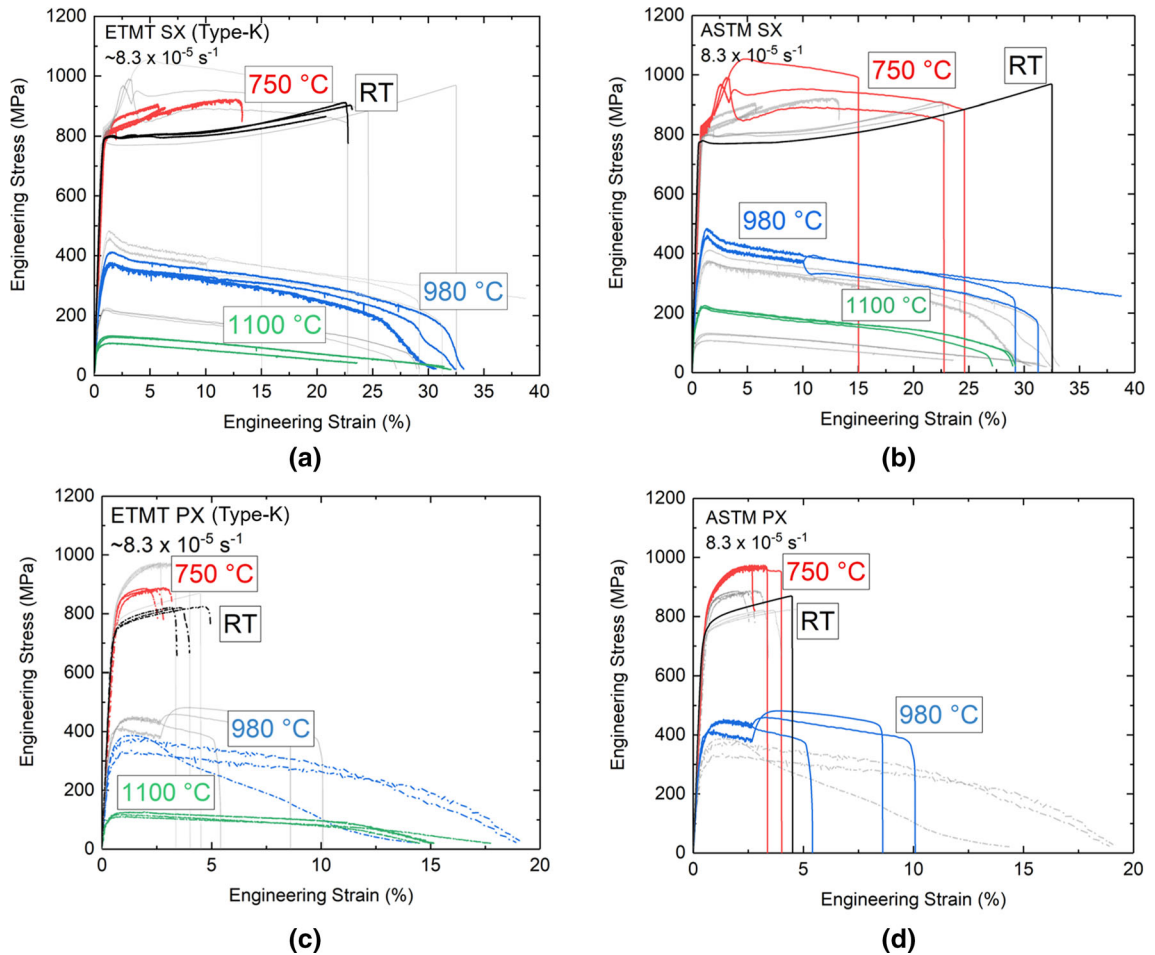


Fig. 1—Engineering stress–strain curves measured using ETMT (Type K T/C) and ASTM procedures for [001] single crystal (a, b) and conventional cast polycrystalline (c, d) Mar-M-247 superalloy. Samples tested at 750 °C using the ETMT approach fractured outside the 3 mm gauge.

C. Microscopy Characterization

Microstructural evolution was characterized using a Zeiss Merlin field emission gun scanning electron microscope (FEG-SEM) with a Bruker electron backscattered diffraction (EBSD) system. Samples were prepared under the standard metallurgical route with 3 minutes of colloidal silica finish. The secondary electron (SE) and backscatter electron (BSE) images were taken under an acceleration voltage of 15 kV. EBSD patterns were stored in 160×120 pixel resolution and subsequently analyzed using ESPRIT 2.3 software. Elemental analysis was conducted using energy-dispersive X-ray spectroscopy (EDS) with an Oxford Instrument X-Max detector for oxidation scale analysis.

IV. RESULTS

A. Tensile Yielding Characteristics

Figure 1 shows the engineering stress–strain curves measured using both approaches. Mechanical response

of [001] SX is illustrated in Figures 1(a) and (b) for ETMT (Type K T/C) and for ASTM, respectively, and PX material response is illustrated in (c) and (d). In general, both methods obtained highly reproducible results in most conditions, where curves overlap from each other for the same technique. To highlight the discrepancies between the two testing methods, figures are presented in the way with both colored and gray scale overlaying each other. For example, Figure 1(a) shows ETMT results in color and the ASTM results in gray scale; *vice versa* for (b). In addition, due to the extensometer being taken off for the ASTM samples after the yield point, only the yielding behavior will be compared in a quantitative manner.

Deformation of SX Mar-M-247 is demonstrated in (a) and (b). At room temperature, the methods produce almost overlapping curves with work hardening characteristics and flow stress showing excellent agreement. The ETMT samples show a slightly lower UTS and a noticeable decrease in the elongation to failure. At 750 °C, the methods determine a comparable flow stress, but the ETMT specimens did not capture the significant

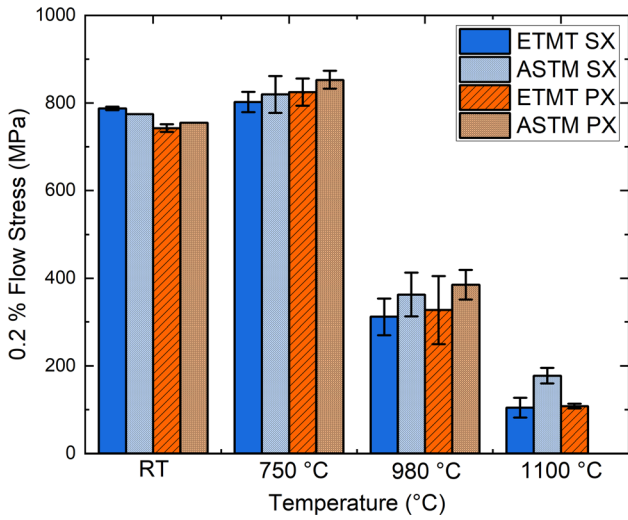
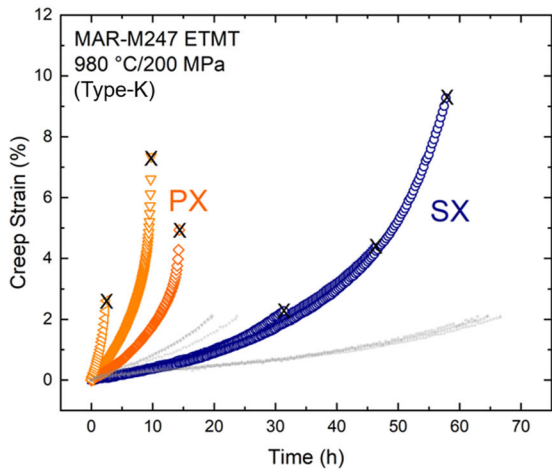


Fig. 2—0.2 Pct offset flow stress comparison between ETMT (Type K T/C) and ASTM for each material from room temperature to 1100 °C. The average value is plotted and spanned with three standard deviations.

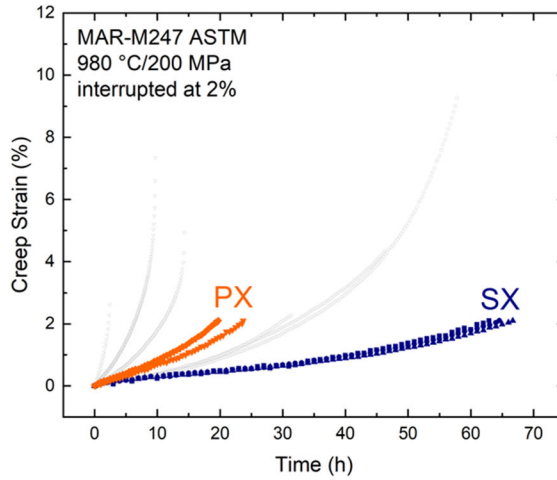
hardening after the yield point as measured by ASTM. In addition, the samples always failed outside the central 3 mm gauge section in this condition. At 980 °C, both methods captured similar stress–strain response, whereas a slightly lower yield strength was obtained by ETMT testing. At 1100 °C, despite each methods provided very repeatable outputs, the flow stress measured by ETMT is significantly lower.

For PX Mar-M-247 see Figures 1(c) and (d), the comparison of stress–strain curves between ETMT and ASTM is broadly similar to these of the SX. In essence, excellent overall agreement at ambient; at 750 °C, the flow stress agrees well but ETMT does not capture the hardening characteristics after yield point; at 980 °C, a slightly lower flow stress is obtained by the ETMT method. Since no ASTM samples were carried out at 1100 °C, no comparison can be made.

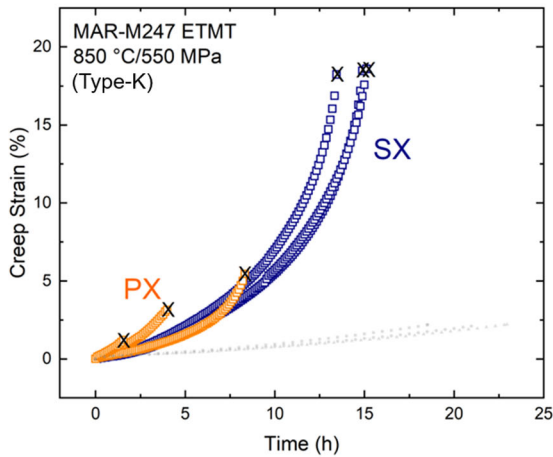
A summary of the 0.2 pct flow stress is shown in Figure 2 spanned in three standard deviation of measurements. It is clear that at least for the measurement of flow stress, both testing reaches good agreement up to 980 °C. Despite a general lower measured flow stress for



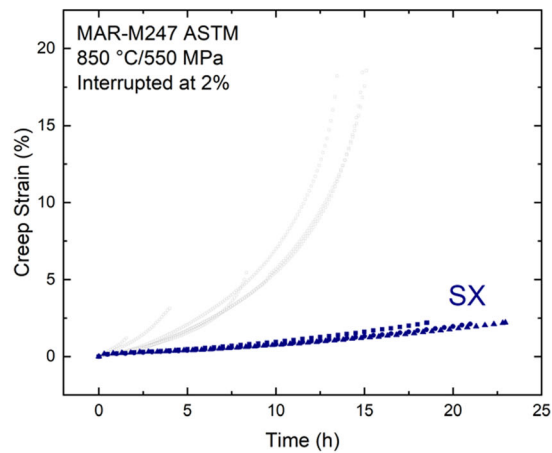
(a)



(b)



(c)



(d)

Fig. 3—Creep rupture curves measured by ETMT with Type K T/C (until fracture) and ASTM (interrupted at 2 pct) approaches at 980 °C/200 MPa (a, b) and 850 °C/550 MPa (c, d).

ETMT, it is within the error range permitted. However, the 1100 °C flow stress measured by ETMT is clearly significantly lower than the ASTM testing; the reasons are rationalized in the discussion section.

B. Creep Deformation

Creep curves at 980 °C/200 MPa and 850 °C/550 MPa are given in Figure 3. For ETMT testing with Type K T/C, Mar-M-247 specimens were taken to failure, where the ASTM samples were interrupted at 2 pct creep strain.

[001] SX Mar-M-247 shows good repeatability between ETMT and ASTM results, but different creep rupture lives. For ETMT, although the creep curves overlap on top of each other, it is worth noting that some experience very different fracture strain at 980 °C/

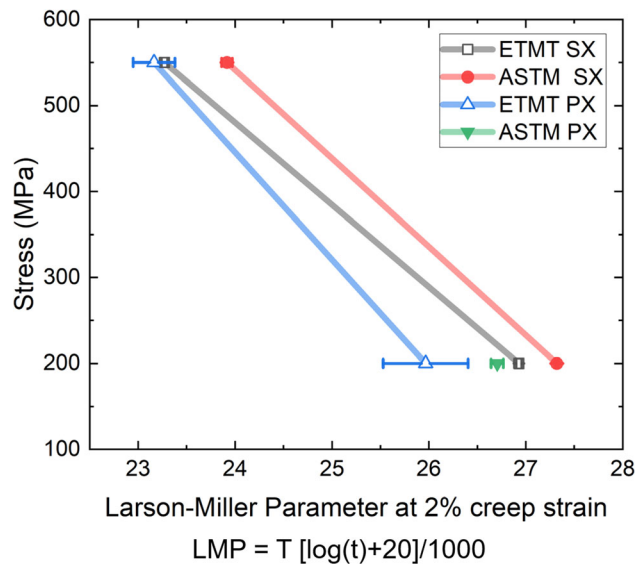


Fig. 4—Larson–Miller Parameter (LMP) plot ($C = 20$) for ETMT (Type K T/C) and ASTM tests using 2 pct creep strain. The average value was spanned with one standard deviation.

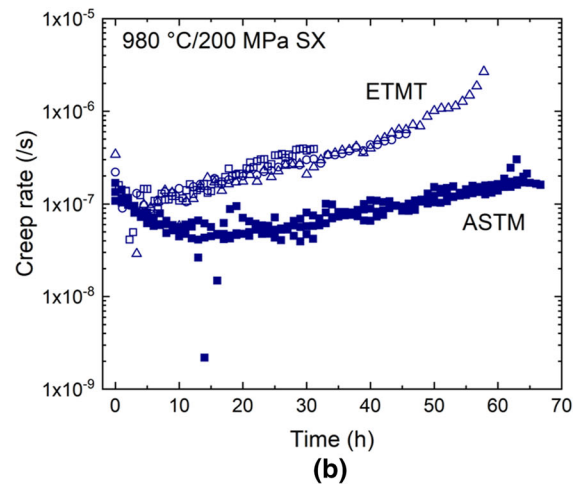
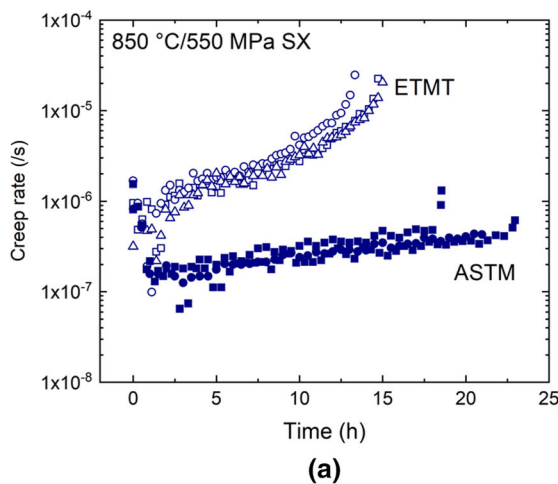


Fig. 5—Instantaneous creep rate for the single crystal Mar-M-247 measured by ETMT (Type K T/C) and ASTM at 980 °C/200 MPa (a) and 850 °C/550 MPa (b).

200 MPa due to premature failure. In addition, the ETMT also underestimates the creep rupture time as opposed to the ASTM method. For example, the ASTM only reaches 2 pct creep strain, whereas the ETMT sample already fractures at 10 pct strain. For PX Mar-M-247, the creep curves scatter significantly for the ETMT testing, whereas the ASTM case, highly reproducible results were obtained. Again, a significantly lower rupture life is measured using the ETMT method.

The creep life results were summarized in a Larson–Miller Parameter (LMP) plot in Figure 4 spanned in one standard deviation. Time to 2 pct creep strain was used for ranking purpose, and the LMP constant was chosen as 20. It is clear that the ETMT system underestimates approximately 0.4 to 0.7 LMP depending on the creep conditions. The closest match was for SX at 980 °C/200 MPa with a $\Delta LMP = 0.39$; the largest deviation was for PX at the same condition with a $\Delta LMP = 0.74$.

Figure 5 demonstrates the instantaneous creep rate for SX Mar-M-247 measured by both techniques. Regardless of testing method or creep conditions, all creep rate vs. time plot shows an initial decrease to minimum creep rate, which it then followed by an increase in rate. Interestingly, the initial creep rates were at the same order of magnitude for both ASTM and ETMT regardless of conditions, *i.e.*, $\sim 1 \times 10^{-6}$ /s for 850 °C/550 MPa and $\sim 1 \times 10^{-7}$ for 980 °C/200 MPa. However, the ETMT creep rate accelerates rapidly after a few hours, and started to deviate largely from the ASTM case by nearly one order of magnitude.

C. Deformation Mechanisms in Creep

Since a large discrepancy was observed in creep testing, further microscopy characterization was used to establish a sound mechanistic understanding of the observed materials behavior.

The largest deviation was observed for PX materials. Figure 6 shows the microstructure from the side

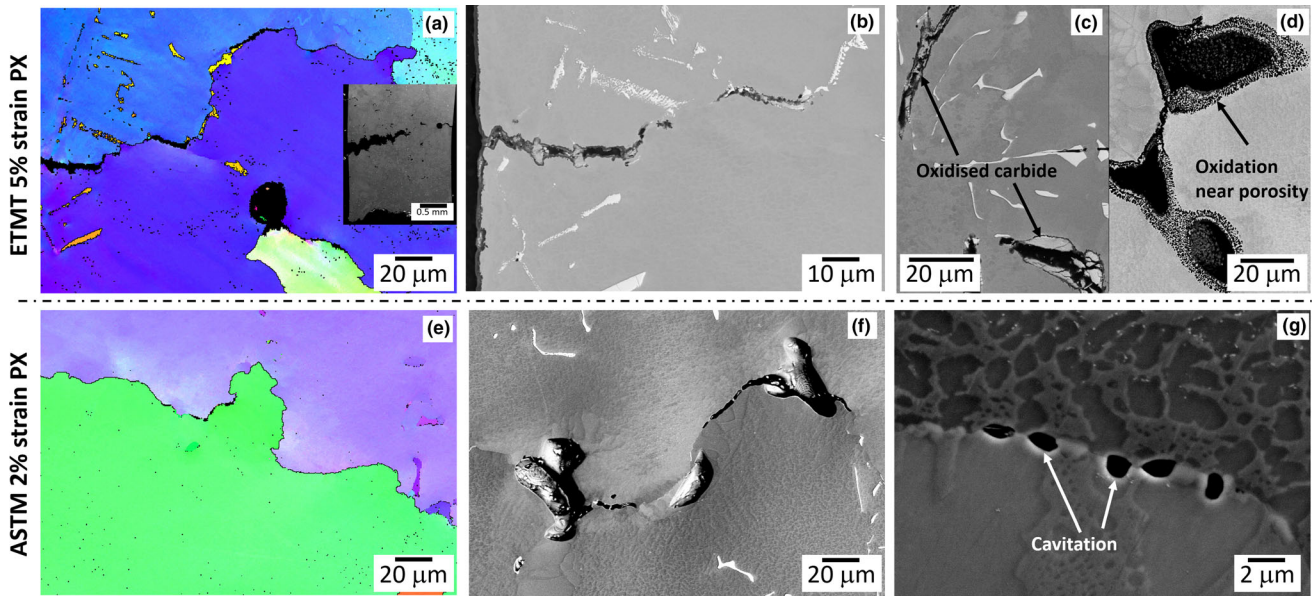


Fig. 6—Microstructural analysis of crept conventional cast polycrystalline Mar-M-247 by ETMT (Type K T/C) which failed at 5 pct strain (*a* through *d*) and ASTM which was interrupted at 2 pct strain (*e* through *g*) at 980 °C/200 MPa.

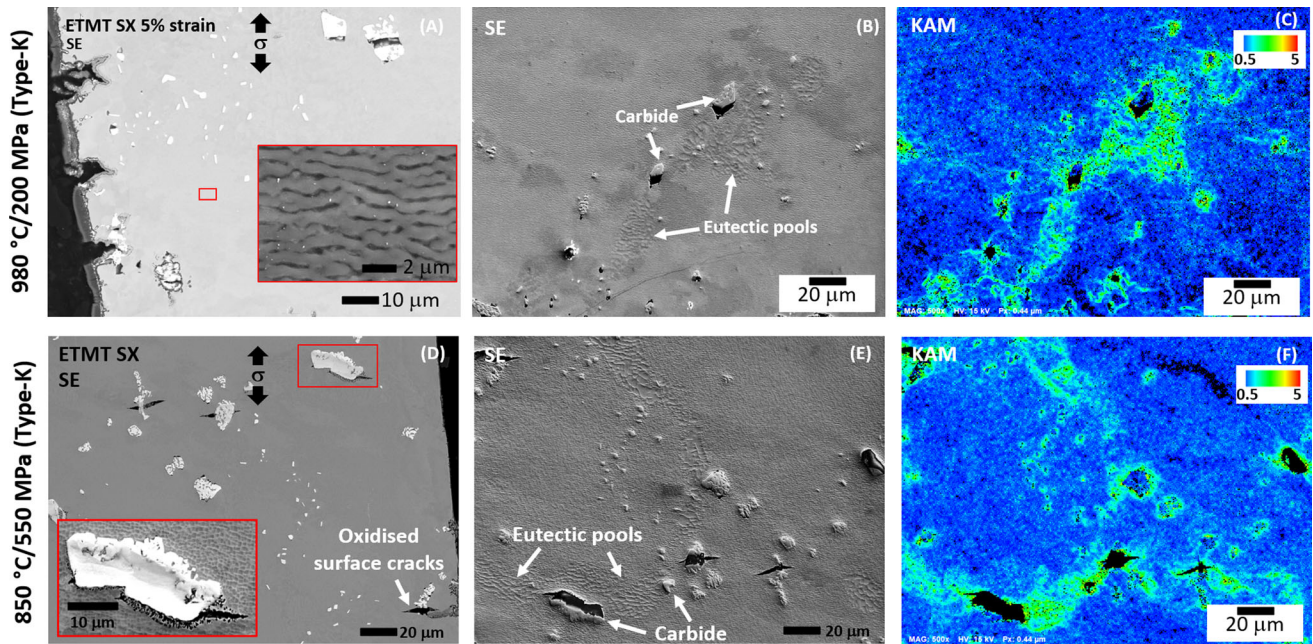


Fig. 7—Microstructural analysis of crept single crystal Mar-M-247 by ETMT (Type K T/C) at 980 °C/200 MPa (*a* through *c*) and 850 °C/550 MPa (*d* through *f*).

cross-section near fracture surface, for both ETMT and ASTM. Large cracking coalescences are observed for the ETMT case, where EBSD confirms the failure is through the grain boundaries. Similar intergranular damage is also found for the ASTM case, whereas only occasional cavitation was found instead of multiple extended crack growth. This does not contribute to an explanation of cracking mechanisms rather it is a manifestation of the level of creep strain (~ 2 pct) it was subjected to. In addition, the ETMT sample shows

extended oxidation along the crack tips, even for some carbides and casting porosities that were not surface connected. On the contrary for the ASTM case, such oxidation was absent even in the vicinity of cavitation and casting porosities.

For the SX Mar-M-247 tested with ETMT, cracking of carbide becomes commonplace. Figures 7(*a*) through (*c*) show multiple crack extension originated from carbide and matrix interfaces in the transverse direction at 850 °C/550 MPa. Kernel average misorientation

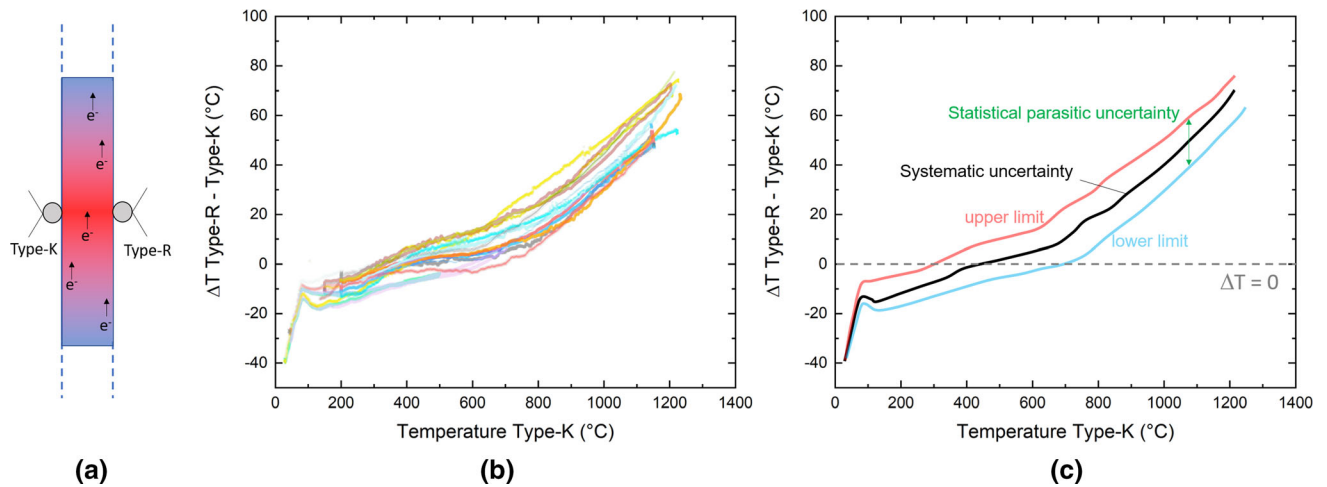


Fig. 8—A statistical approach for verification of temperature uncertainty *via* a dual thermocouple approach. (a) Schematic illustration of the set-up, (b) plot of temperature difference by heating and cooling cycles for 15 specimens and (c) the average with upper and lower bound of temperature uncertainty.

(KAM) map reveals that such cracking induces local misorientation which is exacerbated by the presence of eutectic pools. Similar observations are made to 980 °C/200 MPa as well. However, two new phenomena were observed. First, the material has undergone full γ' -rafting and second, multiple surface connected oxidation cracks were observed at 980 °C/200 MPa. By contrast for the ASTM samples, no such surface cracks were observed; carbide and matrix delamination were not found either. Again, this does not necessarily rationalize the creep behavior due to large differences of the creep strain in each sample.

V. DISCUSSION

Tensile testing carried out by ETMT on $1 \times 1 \text{ mm}^2$ cross-section specimens shows highly reproducible tensile yielding results to those performed in accordance to ASTM procedures—from ambient up to 980 °C for both polycrystalline and SX Mar-M-247. However, a significant underestimation was observed at 1100 °C. Moreover, ETMT creep test demonstrated high repeatability for [001] SX Mar-M-247, but the absolute creep life was markedly underestimated. In addition, ETMT creep test is prone to large scatter for those conventional cast PX material. In what follows, the possible causes for the discrepancy measured will be rationalized *via* a review of various uncertainties and assumptions.

A. Discrepancy Analysis: Uncertainties and Assumptions

1. Temperature accuracy and parasitic voltage

In order to verify the temperature accuracy, specifically the uncertainty of temperature due to the choice of T/C and parasitic voltage that is inherited to the Joule heating method, a statistically approach *via* a dual T/C configuration was proposed, see Figure 8(a). Type K and Type R T/Cs were spot welded to the center of the

gauge section at each side. Thermal cycles from room temperature up to 1250 °C (by Type K control) were carried out for 15 random samples, each were welded with individually made dual T/Cs. Figure 8(b) shows the temperature discrepancy between Type R and Type K against the Type K measurement. From ~ 200 °C up to ~ 750 °C, the two T/Cs obtained very similar reading (within 10 K). It is, however, clear that larger differences are observed at a higher temperature, consistently, the Type R shows a greater value. In the ideal case, *i.e.*, no parasitic voltage or temperature uncertainty, ΔT should be zero. The average of ΔT , *i.e.*, the black curve in Figure 8(c) is considered the systematic uncertainty of the choice of T/C within the temperature range. Although at this point one cannot determine which type of T/C is closer to the true temperature, a certain deviation of measured material's property will be expected when tested using Type K or R.

This forms a plausible explanation to the tensile discrepancy observed at 980 °C and 1100 °C between the two testing methodologies. The Type K T/C has consistently underestimated the local temperature of gauge section, whereas the actual temperature can be approximately 36 °C to 51 °C higher if measured using Type R. It has a significant effect in the microstructures, especially the fraction of the γ' precipitates. According to CALPHAD estimations using TCNI8 database, see Figure 9, the estimated $\Delta\gamma'_f$ is 0.03 at 980 °C and 0.13 at 1100 °C. In order to rectify this, two further ETMT tests were conducted using Type R T/C at 1100 °C, while maintaining other procedures consistent. Figure 10 shows the tensile curves obtained using ETMT Type R and K benchmarked with ASTM testing at 1100 °C. Clearly, tensile results obtained with Type R are much closer to the ASTM case suggesting a more accurate temperature measurement at this condition. The temperature underestimation with Type K T/C also help rationalize the higher creep rate observed for the ETMT

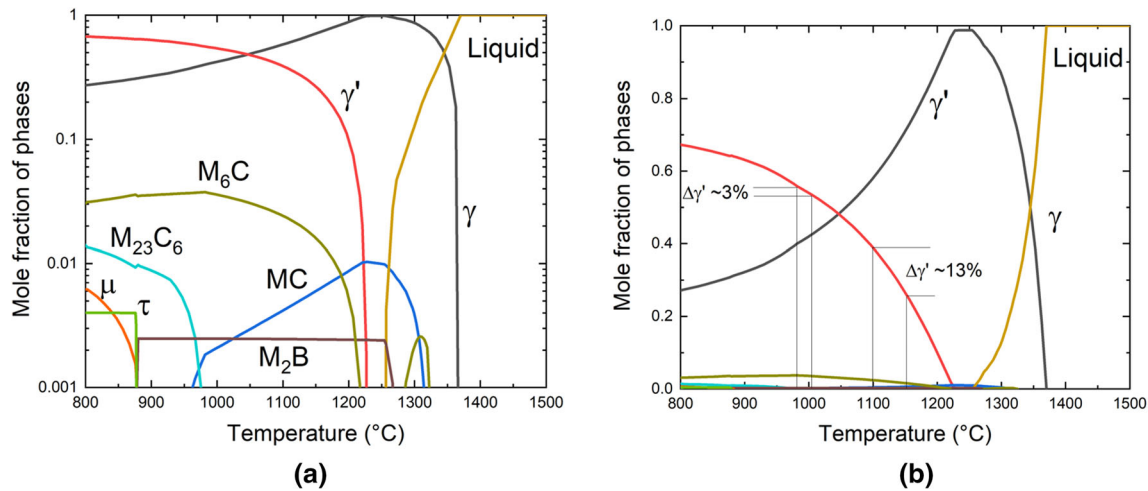


Fig. 9—Equilibrium phase diagram of Mar-M-247 as estimated using CALPHAD approach with TCNI8 database in logarithmic (a) and linear (b) scales.

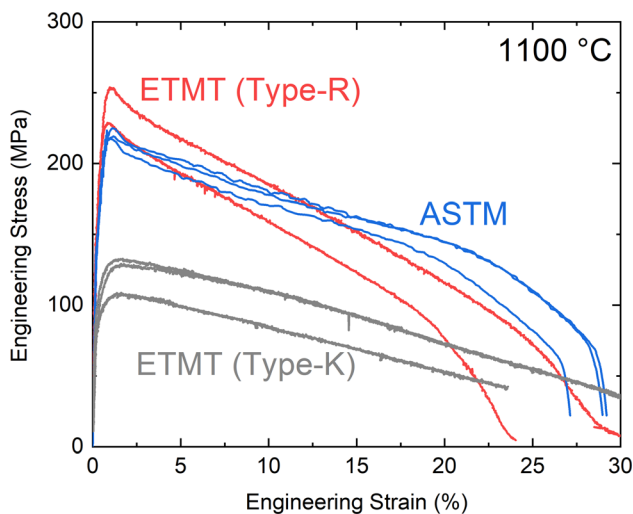


Fig. 10—Tensile testing curves carried out at 1100 °C under ASTM procedures (blue), ETMT with Type K thermocouple (gray) and Type R thermocouple (red) (Color figure online).

approach—a temperature difference of 30 °C can induce a change in creep rate by a factor of 5 or 6.^[29]

Type K T/C was initially chosen for this study due to its large temperature capacity, generally from -200 °C to 1100 °C (with possibility up to 1260 °C). However, there are caveats to it. Type K T/C can suffer from oxidation, typically at 800 °C and above.^[30] The positive leg for Type K is made by Chromel (Ni–10Cr wt pct), where Cr oxides preferentially to form Cr scales. The Cr concentration is then lowered in the base metal that decreases the Seebeck coefficient and measured e.m.f. (electromotive force) values.^[30] Consequently, the T/C reports an underestimated temperature. In the current study, the T/Cs were made in the bare wire configuration without protection from sheath, thus most susceptible to oxidation. The upper temperature limit of oxidation prone T/Cs are often quoted as a function of wire diameter or sheath diameter in manuals,^[31] *i.e.*,

the larger the wire diameter, the higher the temperature limit.^[32]

On the low temperature side, Type R T/Cs are less sensitive due to their very low voltage output (~ 6 $\mu\text{V}/\text{K}$ at room temperature as opposed to ~ 41 $\mu\text{V}/\text{K}$ for Type K), and hence rarely used at below 200 °C in practice. In summary, for bare wire configuration used in the ETMT, Type R T/C should be used at very high temperatures especially when oxidation is significant, but is not the preferred choice for low temperature regime. On the contrary, Type K T/C is reliable up to intermediate temperature; one should be cautious if oxidation can take place. As suggested by the tensile testing data, bare wire Type K should not exceed ~ 980 °C for short-term tests. Type R should be used when oxidation occurs, certainly at 980 °C and beyond.

Parasitic voltage on the other hand, despite its value for each individual T/C is unknown, one can estimate a range by subtracting the upper and lower temperature band in Figure 8(c). If one assumes the temperature uncertainty due to parasitic effect is $\pm x$ K, the difference between the upper and lower band would have captured the statistical contribution of the combined parasitic effect of Type K and Type R, which is measured as approximately 20 K throughout the temperature range. Although this is not a direct measure of parasitic voltage effect, it provides an insight into its significance during a test. Further work on its quantification is needed.

2. Instantaneous strain rate

Another factor with implication to testing results is the strain rate, which was monitored but not controlled using the video extensometer. Instantaneous strain rates at different deformation temperatures are presented in Figure 11, a constant strain rate of $8.3 \times 10^{-5}/\text{s}$ is also shown for reference. It is clear that for all testing a kink (see arrows) is observed for each strain *vs.* time plot—the transition between elastic to plastic regime. For ambient deformation, the strain rate is very close to the ideal value—easy to control as there is no temperature gradient. For high temperature deformation, all

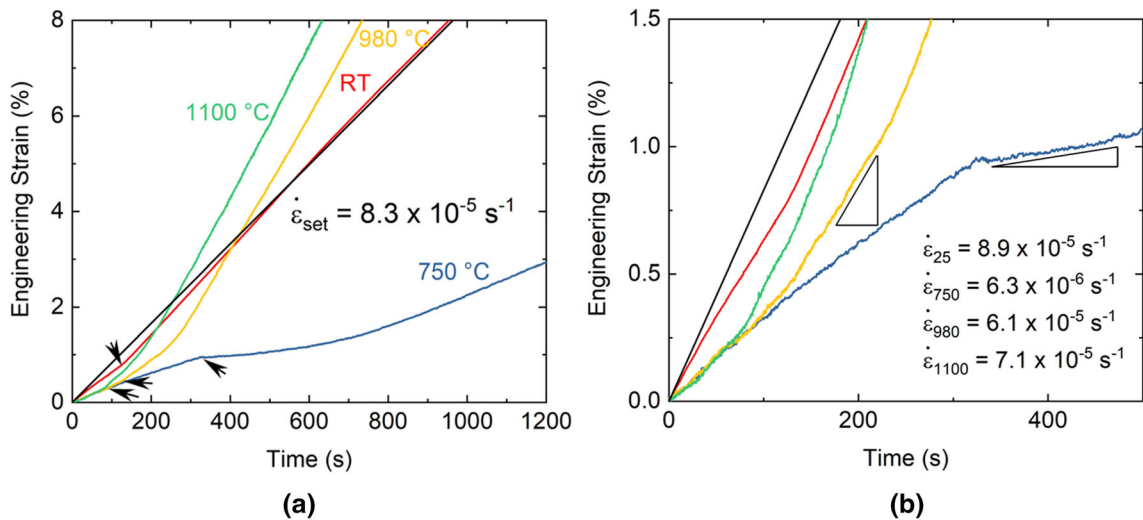


Fig. 11—Actual engineering strain rate of ETMT specimens in both elastic and plastic regime as a function of temperature benchmarked by the set strain rate (a), and a zoomed-in graph to show the initial elastic–plastic transition (b).

tests obtained a lower strain rate at the elastic regime, which then accelerates in the plastic regime. An unusual behavior is observed for the 750 °C case, where a plateau of strain is observed. In this case, further crosshead movement has not yield sufficient deformation at the central gauge anomalous yielding in the non-gauge section at lower temperature deforms instead. After sufficient work hardening in the non-gauge section for a few minutes, the yield transfers back to the central 3 mm gauge which deforms slowly again showing a gradual increase in strain rate. Although the stress–strain response is captured for the gauge, where the load cell and local strain were measured accurately, a significantly lower strain rate at the gauge failed to capture the hardening behavior at 750 °C. Lower strain rate during elevated temperature suggests time allowed for creep relaxation to happen, and hence decreases the flow stress measurement. For example, for a similar alloy CM247LC by additive manufacturing, the flow stress decreased from 843 to 617 MPa when deformed from $\sim 10^{-3}/s$ to $10^{-5}/s$.^[33]

B. Oxidation Kinetics and Joule Heating During Creep

Creep rupture time for ETMT and ASTM demonstrated significant discrepancies, one may intuitively think this is due to the thin-wall debt. In fact, this may not be that significant given the cross-sectional thickness of 2 mm studied here, especially for short-term creep (< 100 hours).^[15] However, one further layer of complication is involved with ETMT creep—microstructural change as a result of Joule heating when electric current density is significant.

With close examination, the oxidation behavior between the ASTM and ETMT samples are markedly different. Figure 12 shows a specimen surface underwent 980 °C/200 MPa creep for 62 hours (ASTM) and 47 hours (ETMT). The oxidation layer thickness for the ASTM is much thinner than the ETMT sample, *i.e.*, ~ 2 vs. $6 \mu\text{m}$. Despite the ETMT sample is likely to be

overheated for 36 K, the difference cannot be explained by this alone. To clarify this, a further oxidation comparison is completed at 1000 °C using conventional resistance furnace and ETMT (Type R) for 100 hours. The oxidation scales are shown in Figure 13, respectively. The scales obtain variable thicknesses. For conventional furnace, this varies between 5 and $10 \mu\text{m}$; for ETMT this varies between 8 and $25 \mu\text{m}$. For representative regions where it shows a uniform thickness, the values are $\sim 7 \mu\text{m}$ for furnace and $\sim 11 \mu\text{m}$ for ETMT. It is also noted that Mar-M-247 contains very high Hf content (1.5 wt pct) which is quite different to many other superalloys. The Hf content is known to alter the oxidation kinetics,^[34] thus the observation may not be universal to Hf-free superalloys.

The difference in oxidation behavior is considered to be induced by the high current density during Joule heating. It is proposed that the accelerated oxidation kinetics is a result of electromigration—a fundamental phenomenon on mass transportation caused by the movement of electrons. This is well known in the semiconductor industry for integrated circuits failures, where the momentum exchange between the electrons colliding with the thermally activated metal ion will exert a force on the metal ion in the direction of electron flow.^[35] Similar to electroplasticity, where electron flow facilitates dislocation mobility, diffusion-controlled oxidation kinetics is altered. For most metals, a current density of 10 to $1000 \text{ A}/\text{mm}^2$ is typical for electroplasticity phenomenon to occur.^[36] During ETMT creep, one obtains a current density of $\sim 2 \times 10^3 \text{ A}/\text{mm}^2$. The rate of mass transfer R due to electromigration can be written in the following form:

$$R \propto J^2 \exp\left(-\frac{\phi}{kT}\right), \quad \square$$

where J is current density ($\text{C}/\text{cm}^2 \text{ s}$), ϕ is activation energy in electron volts, $k = 8.62 \times 10^{-5} \text{ eV}/\text{K}/\text{atom}$, and T is absolute temperature. It is not surprising for

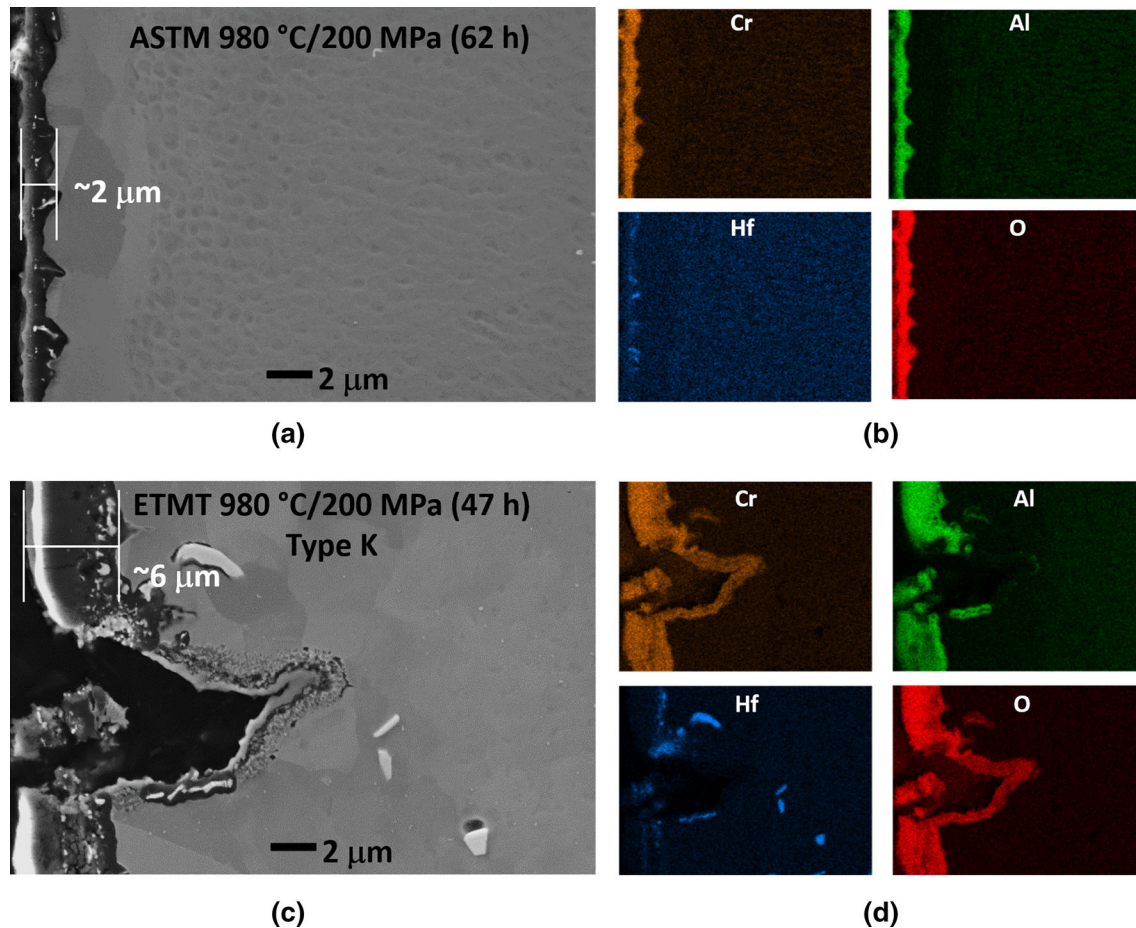


Fig. 12—A comparison between oxidation scales obtained by creep at 980 °C/200 MPa under ASTM (62 hours) in (a and b) vs. ETMT using Type K T/C (47 hours) in (c and d) using SEM imaging and EDS elemental mapping.

nickel to suffer from electromigration to a certain extent due to a combination of significant current density and high temperature. In fact, similar reports on electric current effect induced microstructural change on nickel superalloys are available with similar or lower current densities, such as alteration in the precipitation and recrystallization kinetics,^[37] and growth of intermetallic compound at interfaces.^[38]

The hypothesis on oxidation layer thickening due to electric current effect justifies the material behavior observed, not only a faster creep rate but also the embrittlement effect due to oxidation surface failure. For example at 980 °C/200 MPa, all ETMT creep samples obtained similar creep rate but failed at different levels of strain. It is considered that oxidation-induced surface cracking caused quasi-brittle premature ruptures. Clearly, further research on the Joule heating-induced oxidation and associated implications is needed.

Moreover, one further factor that can potentially contribute to the discrepancy between ASTM and ETMT is the sample geometry, *i.e.*, cylindrical *vs.* flat cross-sections. There are two implications for SX materials, deformation stress state and secondary crystal orientation. The former is prone to alter plastic strain localization behavior,^[39] which is expected to be

more pronounced at the later creep stage. The secondary crystal orientation is known to influence slip patterns and plastic zone sizes, which it consequently changes time-dependent deformation behavior,^[40] such as fatigue.^[41] Sample geometry effect cannot be fully exploited by the current study, it requires more scholarly attention with carefully designed experimentation.

C. Applicability and Limitations

Thus far, a comprehensive study on miniaturized ETMT testing is carried out on quasi-static tensile deformation and creep rupture with SX and PX Mar-M-247, the results are benchmarked by testing employed ASTM procedures.

In general, all tests have demonstrated good repeatability, *i.e.*, small variation between repeats. For tensile yielding behavior, the ETMT has reached good agreement with the ASTM test up to 980 °C with Type K T/C and up to 1100 °C with Type R. Nevertheless, the ETMT has failed to capture the hardening behavior at 750 °C when the anomalous yielding is associated. This is attributed by the strain rate that emerges locally is much lower than the ideal value—stress relaxation *via* creep mechanisms caused such underestimation.

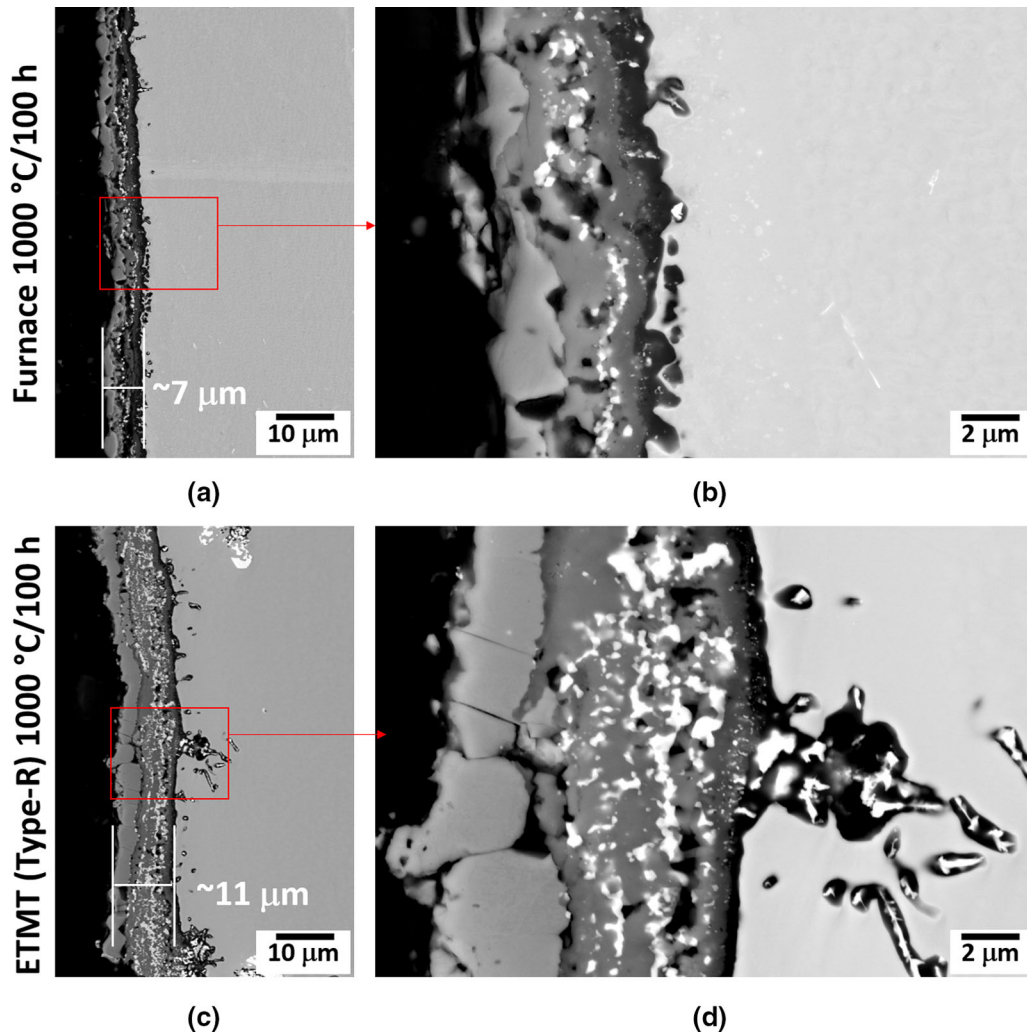


Fig. 13—A comparison between oxidation scales obtained in conventional furnace (*a* and *b*) and ETMT (*c* and *d*) using Type R thermocouple isothermally held at 1000 °C for 100 hours.

Moreover, since the fracture usually happens outside the gauge volume, the ductility is underestimated, too. The hardening at anomalous yield regime may be better captured *via* redesign of sample geometry by reduction of parallel length to provide thicker non-gauge part with improved load bearing capacity. Temperature uncertainty coupled with parasitic voltage effect can be significant at a temperature higher than 800 °C. This is only symptomatic when the microstructure enters a temperature sensitive range, for example, close to γ' solvus point, such as 1100 °C in the current study, or at a lower temperature for Waspaloy.^[42] Grain size on the other hand does not show a very strong effect in repeatability or reproducibility for quasi-static deformation measurement.

On the creep assessment, miniaturized ETMT demonstrates a notable discrepancy in comparison to the ASTM outcome, despite the testing is self-consistent with high repeatability. A significant contribution of this comes from temperature underestimation due to the Type K T/C. In addition to a pure “thin-wall debt”, an

accelerated oxidation effect is also observed in association with the ETMT test. The most plausible hypothesis is the electric current effect that has altered the kinetics. This is only a qualitative measure thus far and robust further research with quantification is needed. However, the electric current effect is likely to influence the materials properties measured only when the test is relatively long. Moreover, the ETMT is not suitable if the sampling volume of grains is not large enough, especially accelerated damage *via* oxidation can occur at grain boundaries.

VI. CONCLUSIONS

This study has involved a comprehensive comparison of the testing of the Mar-M-247 superalloy made using the miniaturized ETMT approach and more standard ASTM procedures. Sources of error, the limitations of

the approaches, and the assumptions inherent in the two techniques are discussed in detail. The following specific conclusions can be drawn from this work:

- (1) The miniaturized ETMT and ASTM tensile tests showed good agreement up to 1100 °C, provided the appropriate type of T/C is chosen. For ETMT specimens, Type K T/C is sufficiently robust until 980 °C, whereas Type R T/C is preferred at higher temperatures.
- (2) In the anomalous yield regime—at a temperature of 750 °C studied here—ETMT testing does not capture the work hardening behavior accurately. This is due to the local strain rate within the gauge being lower than the set value under the displacement control being employed.
- (3) Creep deformation results show a significant discrepancy between ETMT and ASTM methods. The ETMT approach underestimated creep rupture time with Type K T/C and is prone to scatter if the grain size is large in comparison to the gauge volume.
- (4) For SX creep, ETMT de facto captures consistent creep rate with the ASTM test initially and then it accelerates rapidly. It is hypothesized that the root cause of this effect is a combination of temperature uncertainty, sample geometry, and accelerated oxidation kinetics arising *via* the Joule heating effect—this promotes cracks in the oxidation layer which extend into the bulk.
- (5) The ETMT approach can in some instances be prone to a temperature uncertainty. This has been analyzed in detail *via* a bespoke dual T/C set-up. We have seen that the temperature uncertainty associated with parasitic voltage and the choice of T/C becomes notable at 800 °C or higher. The influence of temperature uncertainty is only symptomatic when the microstructure is within a temperature-sensitive range, for example, close to the γ' solvus point.

ACKNOWLEDGMENTS

The authors acknowledge provision of material and funding from MTU Aero Engines AG Germany. YTT and SU would like to thank Andrew Pearce from Instron for technical advice.

CONFLICT OF INTEREST

On behalf of all authors, the corresponding author states that there is no conflict of interest.

OPEN ACCESS

This article is licensed under a Creative Commons Attribution 4.0 International License, which permits use, sharing, adaptation, distribution and reproduction in any medium or format, as long as you give appropriate credit to the original author(s) and the source, provide a link to the Creative Commons licence, and indicate if changes were made. The images or other third party material in this article are included in the article's Creative Commons licence, unless indicated otherwise in a credit line to the material. If material is not included in the article's Creative Commons licence and your intended use is not permitted by statutory regulation or exceeds the permitted use, you will need to obtain permission directly from the copyright holder. To view a copy of this licence, visit <http://creativecommons.org/licenses/by/4.0/>.

REFERENCES

1. V.J. Lyons: *Technology Innovations Magazine*, vol. 15, NASA, Washington, DC, 2009.
2. D. Raabe, C. Tasan, E. Olivetti: *Nature*, 2019, vol. 575, pp. 64–74.
3. H.K. Regina Pouzolz and O. Schmitz: in: *3rd ECATS Conference*, 2020.
4. Airbus: *Hydrogen: An Energy Carrier to Fuel the Climate-Neutral Aviation of Tomorrow*, Airbus, 2021. <https://www.airbus.com/en/innovation/zero-emission/hydrogen>. Accessed 12 Oct 2022.
5. P. Prashanth, R. Speth, S. Eastham, J. Sabnis, and S. Barrett: *Energy Environ. Sci.*, 2021, vol. 14, pp. 916–30.
6. MTU Aero Engines AG: *Water-Enhanced Turbofan*, MTU Aero Engines AG, 2022. <https://www.mtu.de/technologies/clean-air-engine/water-enhanced-turbofan/>. Accessed 12 Oct 2022.
7. MTU Aero Engines AG: *Flying Fuel Cell*, MTU Aero Engines AG, 2022. <https://www.mtu.de/technologies/clean-air-engine/flying-fuel-cell/>. Accessed 12 Oct 2022.
8. Y.T. Tang, N. D'Souza, B. Roebuck, P. Karamched, C. Panwisawas, and D.M. Collins: *Acta Mater.*, 2021, vol. 203, p. 116468.
9. T.B. Gibbons: *Met. Technol.*, 1981, vol. 8, pp. 472–75.
10. J. Doner and M. Heckler: in: *Superalloys*, 1988, pp. 653–62.
11. A. Baldan: *J. Mater. Sci.*, 1995, vol. 30, pp. 6288–98.
12. G. Malzer, R. Hayes, T. Mack, and G. Eggeler: *Metall. Mater. Trans. A*, 2007, vol. 38A, pp. 314–27.
13. M. Bensch, J. Preussner, R. Huttner, G. Obigodi, S. Virtanen, J. Gabel, and U. Glatzel: *Acta Mater.*, 2010, vol. 58, pp. 1607–17.
14. A. Srivastava, S. Gopagoni, A. Needleman, V. Seetharaman, A. Staroselsky, and R. Banerjee: *Acta Mater.*, 2012, vol. 60, pp. 5697–5711.
15. S. Korber, S. Wolff-Goodrich, R. Volkl, and U. Glatzel: *Metals*, 2022, vol. 12, p. 1081.
16. V. Seetharaman and A.D. Cetel: in: *Superalloys 2004*, TMS, K. Green, T. Pollock, H. Harada, T. Howson, R. Reed, J. Schirra, and S. Walston, eds., The Minerals, Metals & Materials Society, 2004, pp. 207–14.
17. B. Cassenti and A. Staroselsky: *Mater. Sci. Eng. A*, 2009, vol. 508, pp. 183–89.
18. L.M. Suave, A.G. Aida Serrano Munoz, G. Benoit, L. Marcin, P. Kontis, P. Villechaise, and J. Cormier: *Metall. Mater. Trans. A*, 2018, vol. 49A, pp. 4012–28.
19. Q. Li, J. Xie, J. Yu, D. Shu, G. Hou, X. Sun, and Y. Zhou: *Prog. Nat. Sci.*, 2022, vol. 32, pp. 104–13.
20. B. Roebuck: *Metallurgia*, 2001, vol. 68, pp. 9–11.
21. B. Roebuck, M. Brooks, and A. Pearce: *Good Practice Guide for Miniature ETMT Tests*, Technical Report 7, National Physical Laboratory, 2016.
22. S. Sulzer, E. Alabort, A. Németh, B. Roebuck, and R. Reed: *Metall. Mater. Trans. A*, 2018, vol. 49A, pp. 4214–35.

23. J.N. Ghoussoub, Y.T. Tang, W.J. Dick-Cleland, A.A. Nemeth, Y. Gong, D.G. McCartney, A.C. Cocks, and R.C. Reed: *Metall. Mater. Trans. A*, 2022, vol. 53A, pp. 962–83.
24. D. Yu, D. Xu, H. Wang, Z. Zhao, G. Wei, and R. Yang: *J. Mater. Sci. Technol.*, 2019, vol. 35, pp. 1039–43.
25. Z.A. Munir, D.V. Quach, and M. Ohyanagi: *J. Am. Ceram. Soc.*, 2011, vol. 94, pp. 1–19.
26. A. Xiao, C. Huang, X. Cui, Z. Yan, and Z. Yu: *J. Alloys Compd.*, 2022, vol. 911, p. 165021.
27. D. Fabregue, B. Mouawad, and C. Hutchinson: *Scripta Mater.*, 2014, vol. 92, p. 3.
28. X. Zhang, H. Li, and M. Zhan: *J. Alloys Compd.*, 2018, vol. 742, pp. 480–89.
29. P. Wollgramm, D. Bürger, A.B. Parsa, K. Neuking, and G. Eggeler: *Mater. High Temp.*, 2016, vol. 33, pp. 346–60.
30. M. Scervini and C. Rae: in: *Proceedings of ASME Turbo Expo 2012*, Copenhagen, Denmark, 2012.
31. Omega Engineering Limited: *Thermocouples: Reference Guide, Booklet*, Omega Engineering Limited, Manchester.
32. M. Scervini: in: *XXI IMEKO World Congress Measurement in Research and Industry*, Prague, Czech Republic, 2015.
33. J.N. Ghoussoub, P. Klups, W.J. Dick-Cleland, K.E. Rankin, S. Utada, P.A. Bagot, D.G. McCartney, Y.T. Tang, and R.C. Reed: *Addit. Manuf.*, 2022, vol. 52, p. 102608.
34. F. Pedraza, R. Troncy, A. Pasquet, J. Delautre, and S. Hamadi: in: *Superalloys 2020*, S. Tin, M. Hardy, J. Clews, J. Cormier, Q. Feng, J. Marcin, C. O'Brien, and A. Suzuki, eds., Springer, Cham, 2020, pp. 408–20.
35. J. Black: in: *2005 43rd Annual IEEE International Reliability Physics Symposium Proceedings*, pp. 1–6, 2005.
36. H. Conrad: *Mater. Sci. Eng. A*, 2000, vol. 287, pp. 227–37.
37. A. Nicolay, J. Franchet, J. Cormier, E. loge, G. Fiorucci, J. Fausty, M.V.D. Meer, and N. Bozzolo: *Metall. Mater. Trans. A*, 2021, vol. 52A, pp. 4572–96.
38. S. Chen, C. Chen, and W. Liu: *J. Electron. Mater.*, 1998, vol. 27, pp. 1193–98.
39. L. Choisez, A. Elmahdy, P. Verleysen, and P. Jacques: *Acta Mater.*, 2021, vol. 220, p. 117294.
40. P. Sabnis, M. Maziere, S. Forest, N.K. Arakere, and F. Ebrahimi: *Int. J. Plast.*, 2012, vol. 28, pp. 102–23.
41. Q.-N. Han, S.-S. Rui, W. Qiu, X. Ma, Y. Su, H. Cui, H. Zhang, and H. Shi: *Acta Mater.*, 2019, vol. 179, pp. 129–41.
42. S. Utada, R. Sasaki, R. Reed, and Y. Tang: *Mater. Des.*, 2022, vol. 221, p. 110911.

Publisher's Note Springer Nature remains neutral with regard to jurisdictional claims in published maps and institutional affiliations.